

Determination of the Equation of State of Dense Matter

Pawel Danielewicz*[†], Roy Lacey[‡] & William G. Lynch*

**NSCL and Department of Physics and Astronomy, Michigan State University, East Lansing MI 48824-1321, USA, [†]Gesellschaft für Schwerionenforschung, 64291 Darmstadt, Germany, and [‡]Department of Chemistry, State University of New York, Stony Brook NY, USA.*

Nuclear collisions have allowed the compression of nuclear matter to densities of up to five times the characteristic central density r_0 of stable nuclei. The dense states of matter exist momentarily before expanding. The flow of matter resulting from this expansion is analyzed to extract pressures in excess of 10^{29} bar, the highest pressures recorded under laboratory-controlled conditions. Here we show that these data rule out very repulsive nuclear equations of state predicted by relativistic nuclear mean field theory and very soft equations of state with a strong phase transition at densities $r < 3r_0$, but not a softening of the equation of state due to a transformation to quark matter at higher densities. Our analysis provides significant constraints relevant to the pressures within neutron stars and within the cores of massive stars during supernovae.

The nucleon-nucleon interaction is generally attractive at separations of $r=1-2$ fm ($1-2 \times 10^{-13}$ cm), but becomes sufficiently repulsive at small separations $r < 0.5$ fm so as to make nuclear matter difficult to compress. As a consequence, most stable nuclei are approximately at the same “saturation” density, $\rho_0 \approx 2.7 \times 10^{14}$ g/cm³, in their interiors, and higher densities do not occur naturally on Earth. Matter at densities of up to $\rho = 9\rho_0$ may be present in the interiors of neutron stars¹ and up to about $\rho = 4\rho_0$ in the core collapse of type II supernovae². The relationship between pressure, density and temperature described by the equation of state (EOS) of dense matter governs the compression achieved in supernovae and neutron stars as

well as their internal structure and many other basic properties¹⁻⁵. Models, which extrapolate the EOS from the properties of nuclei near their normal density and from nucleon-nucleon scattering, are commonly exploited to study such dense systems^{1,3-9}. Consequently, it is important to test these extrapolations by laboratory measurements of high-density matter.

Nuclear collisions provide the only means to compress nuclear matter to high density within a laboratory environment. The pressures that result from the high densities achieved during such collisions influence strongly the motion of ejected matter. This provides the sensitivity to the EOS that is needed for its determination¹⁰⁻¹⁹. The quest for the high-density nuclear EOS has motivated a plethora of theoretical studies¹⁰⁻²⁰ and experimental measurements^{18,21-31} spanning many decades. Only recently, however, have measurements at very high densities become available²³⁻³¹. For such measurements, pressure effects far outweigh the effects of competing phenomena on the sensitive experimental observables, thus allowing the EOS to be determined.

Full equilibrium is not achieved in nuclear collisions relevant to the determination of the EOS. It is therefore necessary to study experimental observables that are associated with the motions of the ejected matter, and to describe them with a dynamical theory. Such theories have been developed to relate experimental observables to the EOS, to distinguish the various microscopic sources of pressure, and to resolve ambiguities in interpretation associated with having more than one source of pressure^{10-14,19} and with other quantities such as the momentum dependent mean field potentials^{10,14}. The results from such analyses can then be extrapolated to determine the corresponding pressures in the equilibrium limit for which the EOS applies. These theoretical developments, combined with the sensitive new measurements, permit the constraints on the EOS that are presented here.

To relate the experimental observables to the EOS and the other microscopic sources of pressure, we apply a model formulated within relativistic Landau theory, which includes both stable and excited (delta, N^*) nucleons (i.e. baryons) as well as pions^{10,13}. It describes the motion of these particles by predicting the time evolution of the (Wigner) one-body phase space distribution functions $f(\mathbf{r}, \mathbf{p}, t)$ for these particles using a set of Boltzmann equations of the form:

$$\frac{\partial f}{\partial t} + (\nabla_{\mathbf{p}} \varepsilon) \cdot (\nabla_{\mathbf{r}} f) - (\nabla_{\mathbf{r}} \varepsilon) \cdot (\nabla_{\mathbf{p}} f) = I. \quad (1)$$

In this expression, $f(\mathbf{r}, \mathbf{p}, t)$ can be viewed semi-classically as the probability of finding a particle, at time t , with momentum \mathbf{p} at position \mathbf{r} . The single particle energies ε in Equation 1 are given in a local frame by

$$\varepsilon = \text{K.E.} + U, \quad (2)$$

where K.E. the kinetic energy and U is the average (mean field) potential, which is computed self-consistently using the distribution functions $f(\mathbf{r}, \mathbf{p}, t)$ that satisfy Equation 1^{10,13}. The particle density is $\rho(\mathbf{r}, t) = \int d\mathbf{p} \cdot f(\mathbf{r}, \mathbf{p}, t)$; the energy density e can be similarly computed from ε and $f(\mathbf{r}, \mathbf{p}, t)$ by carefully avoiding the over-counting of potential energy contributions^{10,13}. The collision integral I on the right hand side of Equation 1 governs the modifications of $f(\mathbf{r}, \mathbf{p}, t)$ by elastic and inelastic two body collisions caused by short-ranged residual interactions^{10,13}.

Compression and expansion dynamics in energetic nucleus-nucleus collisions.

Figure 1 illustrates several aspects of a collision between an Au projectile and an Au target nucleus for an incident kinetic energy of 2 GeV/nucleon (394 GeV). The results, which are shown as a function of elapsed time, have been obtained from a calculation based on the model introduced above^{10,13}. Time increases from left to right in the figure and the left-most

panels depict the nuclei prior to the collision. The trajectories of projectile and target nuclei are displaced relative to a “head-on” collision by an impact parameter of $b=6$ fm (6×10^{-13} cm).

The three dimensional drawings in Figure 1 provide an external view of the collision. When combined with the two dimensional panels, they illustrate the compression and subsequent expansion of nuclear matter following the collision between the projectile and target nuclei. The surfaces in the three dimensional drawings (roughly) correspond to contours of a constant density $\rho=0.1\rho_0$. The magenta arrows in the leftmost panel indicate the initial velocities of the projectile and target. These velocity vectors are collinear with the z -axis in this coordinate system. To make the perspective clear in the other panels, magenta arrows are also used to indicate the corresponding velocities of projectile and target remnants that follow trajectories, which avoid the collision.

The bottom panels show calculated contours of constant density in the reaction plane¹ (the x - z plane in this coordinate system). The outer edge of the dark blue contours corresponds to a density of $0.1\rho_0$. Moving inward, the outer edges of successive contours correspond to steps in density of $0.5\rho_0$; the red regions in the second and third panels (**b'** and **c'**) correspond to densities in excess of $3\rho_0$. The black arrows in both the bottom and the back panels of this figure indicate the average velocities of nucleons at selected points in the (x - z) plane and (x - y) planes, respectively.

The observables sensitive to the EOS are chiefly related to the flow of particles from this high-density region in directions perpendicular (transverse) to the beam axis. This flow is initially zero, but grows with time as the density grows and leads to pressure gradients in directions transverse to the beam axis. The pressure can be calculated in the equilibrium limit by taking the partial derivative of the energy density e with respect to the baryon (primarily nucleon) density ρ :

¹ The reaction plane is defined to be perpendicular to the total orbital angular momentum.

$$P = \rho^2 \cdot \left(\frac{\partial(e/\rho)}{\partial\rho} \right)_{s/\rho}, \quad (3)$$

at constant entropy per nucleon s/ρ in the colliding system. Different theoretical formulations about the energy density would lead to different pressures (i.e. to different equations of state for nuclear matter) in the equilibrium limit, in these simulations and in the actual collisions.

The pressure developed in the simulated collisions is computed microscopically from the pressure-stress tensor, T^{ij} . This tensor is trivially related to the pressure, i.e. $T^{ij} = P\delta^{ij}$, when equilibrium is assumed. (δ^{ij} is the identity matrix.) For non-equilibrium calculations the pressure-stress tensor can be anisotropic and the transverse derivatives of its transverse components provide the driving forces for the transverse acceleration of particles.⁺ In the back panels of Figure 1, we illustrate the pressure gradients that drive these transverse accelerations by plotting the mean transverse pressure $\bar{P}_{tr} = \frac{1}{2}(T^{xx} + T^{yy})$. These panels (**a** – **e**) show contours of constant transverse pressure in the (x-y) plane, which lies perpendicular to the beam axis and contains the center of mass. The outer edge of the dark blue contours corresponds to the edge of the matter distribution where the pressure is essentially zero. Moving inwards, the outer edges of successive contours correspond to steps in pressure of 15 MeV/fm³. (1 MeV/fm³ = 1.6×10^{27} bar, i.e. 1.6×10^{27} atmospheres.)

A maximum central density in excess of $\rho \approx 3\rho_0$ is predicted for the red region visible in the second of the bottom panels, labeled **b'**. The corresponding red region in the back panel, labeled **b**, is at a pressure greater than 90 MeV/fm³. These densities and pressures are

⁺ In non-equilibrium hydrodynamics, the acceleration a^i of matter in direction i is given in its rest frame by the non-equilibrium Euler equation $a^i = -c^2 \partial_j T^{ij} / [e + P']$, where $P' = a^k a^l T^{kl} / (a^m a^m)$. (Note: repeated indices imply summation over the three Cartesian spatial coordinates.)

achieved by inertial confinement. Thus, the incoming matter from both projectile and target is mixed and compressed in the high-density region where the two nuclei overlap. “Participant” nucleons from both projectile and target nuclei, following small impact parameter trajectories (at $x, y \approx 0$), contribute to this mixture by smashing into this compressed region and compressing it further. The calculated transverse pressure in the central region reaches $\sim 80\%$ of its equilibrium value after $\sim 3 \times 10^{-23}$ sec (panel **b'**). The pressure-stress tensor in the same region is equilibrated after $\sim 4 \times 10^{-23}$ sec (panel **c'**) and remains so for the later times represented in Figure 1. Equilibrium is lost at even later times but only after the flow dynamics are essentially complete.

“Spectator” nucleons, which avoid this high density region by following large impact parameter trajectories (with large $|x| > 6$ fm), initially block the escape of compressed matter along trajectories in the reaction plane and force it to flow out of the compressed region in directions perpendicular to the reaction plane. (See back panels **b-d**.) Later, after these spectator nucleons pass, nucleons from the compressed central region preferentially escape along trajectories parallel to the reaction plane that are no longer blocked. This increase of in plane emission is beginning to occur to a limited extent in panel **e** at this incident energy of 2 GeV/nucleon. This later in-plane emission becomes the dominant direction at higher incident energies of 5 GeV/nucleon where the passage time is considerably less. For further orientation, the velocities in the x - y plane are also shown by the red arrows in the three dimensional representations of the collision. Consistent with the back panels, a continuous evolution of the emission in the x - y plane can be seen in the three dimensional representations, from emission along the y -axis (e.g. panel **b**: $t = 30 \times 10^{-24}$ s) and to emission to all directions in the x - y plane (e.g. panel **e**: $t = 50 \times 10^{-24}$ s).

The achievement of such high densities and pressures, coupled with their impact on the motions of ejected particles, provides the sensitivity of collision measurements to the EOS. The directions in which matter expands and flows away from the compressed region depend

primarily upon the timescale for the blockage of emission in the reaction plane by the spectator matter and the timescale for the expansion of the compressed matter near $x \approx y \approx z \approx 0$. The blockage timescale can be approximated by $2R/(\gamma_{cm} v_{cm})$, where R/γ_{cm} is the Lorentz contracted nuclear radius, and v_{cm} and γ_{cm} are the spectator nucleon velocity and the Lorentz factor in the center of mass reference frame. The blockage timescale therefore decreases monotonically with the incident velocity. The expansion timescale can be approximated by R/c_s , where $c_s = c\sqrt{\partial P / \partial e}$ is the sound velocity in the compressed matter and c is velocity of light. The expansion timescale therefore depends (via c_s) upon the energy density e and upon the nuclear mean field potential U according to Equations 2, 3 and their associated discussion. This provides sensitivity to the density dependence of the mean field potential, which is important because uncertainties in the density dependence of the mean field make a dominant contribution to the uncertainty in the EOS. More repulsive mean fields lead to higher pressures and a more rapid expansion when the spectator matter is still present. This causes a preferential emission out of the reaction plane where particles can escape unimpeded. Less repulsive mean fields lead to slower expansion and preferential emission in the reaction plane after the spectators have passed.

Analyses of equation of state dependent observables.

The comparison of in plane to out-of-plane emission rates provides an equation of state (EOS) dependent experimental observable generally labeled as “elliptic flow”. The sideways deflection of spectator nucleons within the reaction plane due to the pressure of the compressed region provides another observable. This sideways deflection, i.e. “transverse flow”, of the spectator fragments occurs primarily while the spectator fragments are adjacent to the compressed region, as shown in the bottom second -fourth panels **b'-d'** of Figure 1. While the velocity arrows in the bottom fourth **d'** and fifth **e'** panels of Figure 1 suggest that the changes in the nucleon momenta, caused by the sideways deflection, are not large, these changes can be extracted precisely from the analysis of emitted particles³². In general, larger

deflections are expected for more repulsive mean fields, which generate larger pressures, and conversely, smaller deflections are expected for less repulsive ones.

In terms of the coordinate system in Figure 1, matter to the right (positive x) of the compressed zone, originating primarily from the projectile, is deflected along the positive x direction and the matter to the left, from the target, is deflected to the negative x direction. Experimentally, one distinguishes spectator matter from the projectile and the target by measuring its rapidity y , a quantity that in the non-relativistic limit reduces to the velocity component v_z along the beam axis.^v When this is done, one observes a monotonic increase in the mean value of the x component of the transverse momentum with increasing values of the rapidity³². Denoting this mean transverse momentum as $\langle p_x \rangle$ and the corresponding transverse momentum per nucleon in the detected particle as $\langle p_x / A \rangle$, one finds that larger values for the pressure in the compressed zone due to more repulsive equations of state lead to larger values for the directed transverse flow F defined by³¹:

$$F = \frac{d\langle p_x / A \rangle}{d(y / y_{cm})} \bigg|_{y / y_{cm} = 1}, \quad (4)$$

where y_{cm} is the rapidity of particles at rest in the center of mass and A is the number of nucleons in the detected particle. (F can be viewed qualitatively as the tangent of the mean angle of deflection in the reaction plane. Larger values for F correspond to larger deflections.) The open and solid points in Figure 2 shows measured values for the directed transverse flow in collisions of ¹⁹⁷Au projectile and target nuclei at incident kinetic energies E_{beam}/A ranging from about 0.15 to 10 GeV/nucleon (29.6 – 1970 GeV total beam kinetic energies) and at impact parameters of $b=5-7$ fm ($5-7 \times 10^{-13}$ cm)²³⁻²⁶. The scale at the top of this figure

^v The rapidity y is defined by $y = \frac{1}{2} \ln \left(\frac{E + p_z c}{E - p_z c} \right)$, where c is the speed of light, p_z is the momentum component parallel to the beam axis and E is the total energy of the particle (including the rest mass). It is additive under Lorentz transformations along the beam direction and reduces non-relativistically to v_z/c .

provides theoretical estimates for the maximum densities achieved at selected incident energies. The maximum density increases with incident energy; the flow data are most strongly influenced by pressures corresponding to densities that are somewhat less than these maximum values.

The data display a broad maximum centered at an incident energy of about 2 GeV/nucleon. The short dashed curve labeled “cascade” shows predictions for the transverse flow predicted by Equation 1 when the repulsive mean field at high density is neglected. The disagreement of this curve with the data shows that a repulsive mean field at high density is needed to reproduce these experimental results. The other curves correspond to predictions using Equation 1 and mean field potentials of the form

$$U = (a\rho + b\rho^v) / (1 + [0.4\rho/\rho_0]^{v-1}). \quad (5)$$

Here, the constants a , b and v are chosen to reproduce the binding energy and the saturation density of nuclear matter while providing different dependencies on density at much higher density values. These curves are labeled by the curvature $K \equiv 9dp/d\rho|_{s/\rho}$ of each EOS about the saturation density ρ_0 . Calculations with these mean fields and larger values of K generate larger transverse flows because the mean fields with larger K generate higher pressures at high density. The labels “less pressure” and “more pressure” in the figure emphasize this relationship between flow and pressure. The precise values for the pressure at high density depends on the exact form chosen for U . To illustrate the dependence of pressure on K for these EOS’s, we show the pressure for zero temperature symmetric matter predicted by the EOS’s with $K=210$ and 300 MeV in Figure 3, as the thin red and thick green lines respectively. The EOS with $K=300$ MeV generates about 60% more pressure than the one with $K=210$ MeV at densities of $2-5\rho_0$. Other theoretical curves and a crosshatched region are also shown in Figure 3; these are explained in the discussion section below.

Corresponding information can be obtained from the in-plane vs. out-of-plane emission (elliptic flow) by measuring the average value $\langle \cos 2\varphi \rangle$ for protons, where φ is the azimuthal angle of the proton momentum relative to the x-axis defined in Figure 1.^{11,12,33} (Here, $\tan \varphi = p_y / p_x$, where p_x and p_y are the in-plane and out-of-plane components of the momentum perpendicular to the beam.). Experimental determinations of $\langle \cos 2\varphi \rangle$ include particles that, in the center of mass frame, have small values for the rapidity y and move mainly in directions perpendicular to the beam axis. Negative values for $\langle \cos 2\varphi \rangle$ indicate that more protons are emitted out-of-plane ($\varphi \approx 90^\circ$ or $\varphi \approx 270^\circ$) than in-plane ($\varphi \approx 0^\circ$ or $\varphi \approx 180^\circ$), and positive values for $\langle \cos 2\varphi \rangle$ indicate the reverse situation.

Experimental values for $\langle \cos 2\varphi \rangle$ are shown in Figure 4 for incident kinetic energies E_{beam}/A ranging from 0.4 to 10 GeV/nucleon (78.8 – 1970 GeV total beam kinetic energies) and at impact parameters of $b=5-7$ fm ($5-7 \times 10^{-13}$ cm)²⁷⁻²⁹. Negative values for $\langle \cos 2\varphi \rangle$, reflecting a preferential out-of-plane emission, are observed at energies below 4 GeV/A indicating that the compressed region expands while the spectator matter is present and blocks the in-plane emission. Positive values for $\langle \cos 2\varphi \rangle$, reflecting a preferential in-plane emission, are observed at higher incident energies, indicating that the expansion occurs after the spectator matter has passed the compressed zone. The various curves provide the corresponding predictions using Equation 1 and the same family of equations of state that are used in Figure 2. Calculations without a mean field, labeled “cascade”, provide the most positive values for $\langle \cos 2\varphi \rangle$. More repulsive, higher pressure EOS’s with larger values of K provide more negative values for $\langle \cos 2\varphi \rangle$ at incident energies below 5 GeV/nucleon, reflecting a faster expansion and more blocking by the spectator matter while it is present. The labels “less pressure” and “more pressure” in the figure emphasize this relationship between elliptic flow and pressure. The scale at the top of this figure provides theoretical estimates for the maximum densities achieved at selected incident energies..

Constraints on the symmetric matter equation of state.

Figures 2 and 4 show that both elliptic and transverse flow observables are highly sensitive to the mean field and to the equation of state at central densities of $2-5\rho_0$. In comparing the two observables to the calculations, one does not find a unique formulation of the EOS that reproduces all data. At incident energies of 2-6 GeV/A, for example, the transverse flow data lie near or somewhat below (to the low pressure side of) the $K=210$ MeV calculations, while the elliptic flow data lie closer to the $K=300$ MeV calculations. Some discrepancies are also observed between the two sets of experimental transverse data at incident energies of 0.25-0.8 GeV/A. While it is not possible to fully resolve the inconsistencies between theory and experiment at the present time, one can use these data to provide new and significant constraints on the EOS. For example, calculations without a mean field (cascade) or with a weakly repulsive mean field ($K=167$ MeV) provide too little pressure to reproduce either flow observable at higher incident energies (and correspondingly higher densities). The transverse flow data approach the $K=167$ MeV calculation at low energies (and lower densities), but the sensitivity of transverse flow to the EOS is weak at low energies where it is sometimes comparable to the differences between the two data sets. We therefore do not place strong constraints on the pressure at $\rho/\rho_0 < 2$ at the present time. The calculation with $K=380$ MeV generally produces too much pressure to reproduce either transverse and elliptic flow; it only approaches the average trends of the data at energies where the calculations with different equations of state differ little and the sensitivity of the flow to the EOS is small. The calculations with $K=167$ MeV and $K=380$ MeV therefore provide clear lower and upper bounds on the pressure in the density range $2 \leq \rho/\rho_0 \leq 5$. Indeed, these comparisons suggest that the upper bound must lie lower than the pressures corresponding to the $K=380$ MeV curve at most densities and that a field that is less repulsive than $K=380$ MeV at densities $\rho > 3\rho_0$ could provide a stricter upper bound on the pressure. We return to the constraints these data place on the equation of state in the discussion section.

It is interesting to note that our calculations provide a calibration for the transverse and elliptic flow “barometers”. These can be used, in turn, to assess the pressures achieved in the

hot and non-equilibrium environment of a nuclear collision. Using transport theory, for example, we determine that maximum pressures in the range of $P = 80\text{-}130 \text{ MeV/fm}^3$ ($1.3\text{-}2.1 \times 10^{29} \text{ bar}$) and $P = 210\text{-}350 \text{ MeV/fm}^3$ ($3.4\text{-}5.6 \times 10^{29} \text{ bar}$) are achieved at incident energies of 2 and 6 GeV/nucleon. These pressures are approximately 23 orders of magnitude larger than the maximum pressures recorded previously under laboratory-controlled conditions³⁴. They are roughly 19 orders of magnitude larger than pressures within the Solar core, but comparable to pressures within neutron stars.

One factor limiting the precision of past analyses of flow data is that both transverse and elliptic flows are also sensitive to the momentum dependencies of the nuclear mean fields and to the uncertainties in the scattering by the residual interaction within the collision term I in Equation 1. The global flow observables in Figures 2 and 4 do not suffice to constrain several uncertainties at once and additional information is needed. While the momentum dependence of the mean field at normal density ρ_0 can be directly studied in nucleon-nucleus scattering, constraints upon the momentum dependence of the mean fields at supranormal densities have only recently been obtained through investigations of experimental observables^{10,14} such as the momentum dependence of $\langle \cos 2\varphi \rangle$ for peripheral collisions, where matter is less compressed than in central collisions. Figure 5 shows experimental values of $\langle \cos 2\varphi \rangle$ for protons³ detected at values of the rapidity $0.35 \leq y/y_{beam} \leq 0.65$, close to that of the center of mass, as a function of the transverse component, p_{\perp} , of the proton momentum. The various curves correspond to solutions of Equation 1 for different assumptions about the momentum dependence¹⁰ and are labeled by the nucleon effective mass corresponding to that momentum dependence. Smaller effective masses lead to a more rapid nucleonic motion, a rapid emission from the overlap region while the spectator matter is present and consequently, more negative values for $\langle \cos 2\varphi \rangle$.

The available data³⁰ constrain the mean-field momentum dependence up to the density of about $2\rho_0$. In the calculations in Figures 2-4, we use the momentum dependence

characterized by $m^*=0.7m_N$, where m_N is the free nucleon mass, and extrapolate this dependence to still higher densities. This choice is consistent with nucleon scattering and the analyses by Danielewicz¹⁰ of the data of Brill *et al.*³⁰. We also make density dependent in-medium modifications to the free nucleon cross-sections following Danielewicz¹⁰ and constrain these modifications using observables characterizing stopping in collisions, including the longitudinal momentum distributions (p_z distributions) of reaction products.

Determination of constraints and comparison to theoretical equations of state.

Comparing calculations and data of Figures 2 and 4 and factoring in the uncertainties due to the momentum dependencies of the mean fields and the collision integral, we have assessed the range of pressure-density relationships that are allowed by the data. These are shown for densities of $2 < \rho / \rho_0 < 4.6$ and, following tradition, zero temperature matter by the shaded region in Figure 3. These bounds on the equation of state for symmetric nuclear matter are the main achievement of this work. In extrapolating to cold matter, we must take the difference between the zero and finite-temperature matter into account. This correction depends on the included excited particle states and the properties of these excited states become increasingly uncertain as excitation energy increases. Surprisingly, however, the uncertainty introduced by this correction remains small because nonstrange baryons with known properties are the dominant species at high densities in these collisions and they dominate the pressure. The limited uncertainty in the pressure due the inclusion of the excited states is included in the bounds in Figure 3. We expect future investigations, which reduce the uncertainties in the experimental data and in the theoretical calculations, can narrow these bounds considerably. Nevertheless, these first bounds on the equation of state can provide significant constraints on theoretical models.

It is interesting to compare our results with conclusions reached by other researchers. Sahu *et al.*¹⁵ have also interpreted the collective flow data with their transport model; they best reproduce the data with an EOS that is contained within the shaded region in Figure 3 at all

densities except for $\rho \leq 2.5\rho_0$, where their EOS was not optimized. B.-A. Li et al.¹⁶ have calculated some flow observables with momentum *independent* mean fields; this lack of momentum dependence makes comparisons with their calculations difficult. On the other hand, their flow results without a mean field generally agree with ours and with other similar calculations in the literature^{15,16,26,35}. Finally, we note that the EOS deduced from kaon production in nuclear collisions²⁰ lies within the shaded region in Figure 3, even though kaon production is less directly related to the pressure achieved in the dense region.

To illustrate the value of these constraints, a few representative theoretical EOS's are shown in Figure 3 for comparison purposes. The EOS of Akmal et al. (dashed-dotted black line)³, which passes through the allowed region, represents a class of models that take the two-nucleon interactions from fits to nucleon-nucleon scattering data. The EOS of Lalazissis et al.⁶ (thick dashed blue-green line) represents a class of relativistic mean field theory models that derive the nucleon-nucleon interaction from the exchange of effective ω and σ mesons. While most such models provide too much pressure, we note that a recent inclusion by Typel and Wolter⁷ of non-linear terms in the Lagrangian can reduce the pressure in such models so as to be consistent with the present experimental constraints. The EOS of Boguta (thin dashed magenta line)³⁶ illustrates the softening of the EOS that might occur if there were another phase more stable than nuclear matter for densities of about $3\rho_0$. Both it and the calculation without mean field (small-dashed blue line) produce too little pressure. On the other hand, an EOS that increases in pressure consistent with these constraints, e.g. the Akmal EOS, and then remains constant with density above $\rho/\rho_0 = 3$ consistent with the existence of a different, more stable, phase at higher densities $\rho/\rho_0 > 4$, e.g. the quark-gluon plasma, cannot be precluded by the present analysis.

These constraints on the EOS of symmetric matter are very relevant to the dynamics of supernovae and to the properties of neutron stars where such densities are achieved¹. Supernovae involve admixtures of neutrons and protons that are similar to the Au+Au system;

the application of these constraints to supernovae is more straightforward than is the application of these constraints to extremely neutron-rich environments like neutron matter or neutron stars. In such neutron rich environments, one must consider how the equation of state depends on the difference between the neutron and proton concentrations. This concentration difference vanishes for symmetric matter, but in pure neutron matter gives rise to an additional source of pressure $P_{\text{sym}} = \rho^2 d(E_{\text{sym}}(\rho))/d\rho \Big|_{s/\rho}$, which depends on the symmetry energy $E_{\text{sym}}(\rho)$. The symmetry energy determines how the energies of nuclei and nuclear matter depend on the difference between neutron and proton densities. This energy is repulsive and is the reason why light nuclei have nearly equal numbers of protons and neutrons. However, few experimental constraints on the density dependence of $E_{\text{sym}}(\rho)$ exist. Therefore, we employ, in the following, two parameterizations for $E_{\text{sym}}(\rho)$ proposed by Prakash *et al.*⁴ to assess the sensitivity of neutron star properties to the asymmetry term.

The violet shaded (Exp+Asy_stiff) region shows the extrapolation of the allowed region from Figure 3, assuming an asymmetry term (labeled F_1 by Li *et al.*³⁷) that has a strong density dependence. The cross-hatched (Exp+Asy_soft) region shows the corresponding prediction assuming an asymmetry term (labeled F_3 by Li *et al.*³⁷) with a weak density dependence. Clearly, the uncertainty in the pressure due to the asymmetry term, represented by the difference between the pressures for these two “allowed” regions, exceeds the remaining uncertainty in the pressure due to the symmetric matter EOS, represented by the width of each region. One should note that the pressure in the actual neutron star environment would be somewhat smaller reflecting the small fraction of nucleons that are protons. The precise values of this proton fraction and many other static and dynamical properties of these dense astrophysical objects depend on the density dependence of the asymmetry term⁴.

The theoretical curves in Figure 6 show the predictions of a variety of theoretical predictions for the neutron matter equation of state^{3,5,8,9}. The small-dashed blue line for a pure Fermi gas indicates that the Fermi motion of nucleons supplies comparatively little pressure;

the repulsive mean field potential supplies most of the pressure. The EOS of Akmal et al. (dashed-dotted black line)³ and the av14uv11 EOS of Wiringa (thin red line)⁸ are both models that take the two-nucleon interactions from fits to nucleon-nucleon scattering data. The EOS of Müller and Serot et al.⁹ (thick dashed blue-green line) represents a class of relativistic mean field theory models that derive the nucleon-nucleon interaction from the exchange of effective ω and σ mesons. Its prediction is essentially the same as the neutron matter predictions for the model of Lalazissis et al.,⁶ (labeled NL3 in Figure 3). While these models appear to provide too much pressure, other relativistic mean field theory models of Müller and Serot et al.⁹ and the calculations of Glendenning et al.⁵, shown by the green line, predict lower pressures. Clearly, the uncertainty in the pressure due to the asymmetry term widens the range of possible equations of state that may be consistent with the experimental data. For this purpose it is important to obtain experimental constraints on the asymmetry term³⁷⁻⁴⁰ and to complement them with improved constraints on the EOS of symmetric nuclear matter.

In summary, we have analyzed the flow of matter in nuclear collisions to determine the pressures attained at densities ranging from two to five times the saturation density of nuclear matter. We obtain constraints on the equation of state of symmetric nuclear matter that rule out very repulsive equations of state from relativistic mean field theory, very soft equations of state with a strong phase transition at densities $\rho < 3\rho_0$, but not a softening of the equation of state due to a transformation to quark matter at higher densities. Investigations of the asymmetry term of the equation of state are important to complement our constraints on the symmetric nuclear matter equation of state. Both measurements relevant to the asymmetry term and improved constraints on the equation of state for symmetric matter appear feasible; they can provide the experimental basis for constraining the properties of dense neutron-rich matter and dense astrophysical objects like neutron stars.

1. Lattimer, J.M. and Prakash, M., Neutron star structure and the equation of state, *Ap. J.* **550**, 426 (2001).
2. Bethe, H.A., Supernova mechanism, *Rev. Mod. Phys.* **62**, 801 (1990).
3. Akmal, A., Pandharipande, V. R., and Ravenhall, D. G., Equation of state of nucleon matter and neutron star structure, *Phys. Rev. C* **58**, 1804 (1998).
4. Prakash, M., Ainsworth, T.L. and Lattimer, J.M., Equation of state and the maximum mass of neutron stars, *Phys. Rev. Lett.* **61**, 2518 (1988).
5. Glendenning, N. K., Weber, F. and Moszkowski, S. A., Neutron stars in the derivative coupling model, *Phys. Rev. C* **45**, 844 (1992).
6. Lalazissis, G. A., König, J. and Ring, P., New parametrization for the Lagrangian density of relativistic mean field theory, *Phys. Rev. C* **55**, 540 (1997).
7. Typel, S. and Wolter, H.H., Relativistic mean field calculations with density-dependent meson-nucleon coupling, *Nucl. Phys. A* **656**, 331 (1999).
8. Wiringa, R. B., Fiks, V. and Fabrocini, A., Equation of state for dense nucleon matter, *Phys. Rev. C* **38**, 1010 (1988).
9. Muller, H. and Serot, B.D., Relativistic mean-field theory and the high-density nuclear equation of state, *Nucl. Phys. A* **606**, 508 (1996).
10. Danielewicz, P., Determination of the mean-field momentum-dependence using elliptic flow, *Nucl. Phys. A* **673**, 375 (2000).
11. Danielewicz, P., Effects of compression and collective expansion on particle emission from central heavy-ion reactions, *Phys. Rev. C* **51**, 716 (1995).

12. Sorge, H., Elliptic flow: a signature for early pressure in ultrarelativistic nucleus-nucleus collisions, *Phys. Rev. Lett.* **78**, 2309 (1997).
13. Bertsch, G. and Das Gupta, S., A guide to microscopic models of intermediate energy heavy ion collisions, *Phys. Rep.* **160**, 189 (1988).
14. Pan, Q. and Danielewicz, P., From sideward flow to nuclear compressibility, *Phys. Rev. Lett.* **70**, 2062 (1993).
15. Sahu, P.K., Hombach, A., Cassing, W., Effenberger, M. and Mosel, U., Baryon flow at SIS energies and beyond, *Nucl. Phys. A* **640**, 493 (1998); Sahu, P.K., Cassing, W., Mosel, U. and Ohnishi, A., Baryon flow from SIS to AGS energies, *Nucl. Phys. A* **672**, 376 (2000).
16. Li, B.-A. and Ko, C.M., Formation of superdense hadronic matter in high energy heavy-ion collisions, *Phys. Rev. C* **52**, 2037 (1995); Li, B.-A. and Ko, C.M., Probing the softest region of the nuclear equation of state, *Phys. Rev. C* **58**, R1382 (1998).
17. Scheid, W., Müller, H. and Greiner, W., Nuclear Shock Waves in Heavy-Ion Collisions, *Phys. Rev. Lett.* **32**, 741 (1974).
18. Reisdorf, W. and Ritter, H.G., Collective flow in heavy-ion collisions, *Ann. Rev. Nucl. Part. Sci.* **47**, 663 (1997).
19. Stocker, H. and Greiner, W., High-energy heavy-ion collisions - Probing the equation of state of highly excited hadronic matter, *Phys. Rep.* **137**, 277 (1986).
20. Fuchs, C., Faessler, A., Zabrodin, E. and Zheng, Y.-M., Probing the Nuclear Equation of State by K⁺ Production in Heavy-Ion Collisions, *Phys. Rev. Lett.* **86**, 1974 (2001).

21. H. A. Gustafsson, *et al.*, Collective Flow Observed in Relativistic Nuclear Collisions, *Phys. Rev. Lett.* **52**, 1590 (1984).
22. R. E. Renfordt, *et al.*, Stopping Power and Collective Flow of Nuclear Matter in the Reaction Ar+Pb at 0.8 GeV/u, *Phys. Rev. Lett.* **53**, 763 (1984).
23. Gustafsson, H.A. *et al.*, Energy and multiplicity dependence of fragment flow in high-energy nuclear collisions, *Mod. Phys. Lett. A* **3**, 1323 (1988).
24. Partlan, M.D. *et al.*, Fragment flow in Au+Au collisions, *Phys. Rev. Lett.* **75**, 2100 (1995).
25. Barrette, J. *et al.*, Proton and pion production relative to the reaction plane in Au + Au collisions at 11 A GeV/c, *Phys. Rev. C* **56**, 3254 (1997).
26. Liu, H. *et al.*, Sideward flow in Au + Au Collisions between 2A and 8A GeV, *Phys. Rev. Lett.* **84**, 5488 (2000).
27. Gutbrod, H.H. *et al.*, A new component of the collective flow in relativistic heavy-ion collisions, *Phys. Lett. B* **216**, 267 (1989).
28. Pinkenburg, C. *et al.*, Elliptic flow: transition from out-of-plane to in-plane emission in Au+ Au collisions, *Phys. Rev. Lett.* **83** 1295 (1999).
29. Braun-Munzinger, P. and Stachel, J., Dynamics of ultra-relativistic nuclear collisions with heavy beams: an experimental overview, *Nucl. Phys. A* **638**, 3c (1998).
30. Brill, D. *et al.*, Study of the out-of-plane emission of protons and light fragments in symmetric heavy-ion collisions , *Zeit. f. Phys. A* **355**, 61 (1996).

31. Doss, K.G. R. *et al.*, Nuclear collective flow as a function of projectile energy and mass, *Phys. Rev. Lett.* **57**, 302 (1986).
32. Danielewicz, P. and Odyniec, G., Transverse momentum analysis of collective motion in relativistic nuclear collisions, *Phys. Lett. B* **157**, 146 (1985).
33. Ollitrault, J.-Y., Anisotropy as a signature of transverse collective flow, *Phys. Rev. D* **46**, 229 (1992).
34. Badro, J., *et al.*, Magnetism in FeO at megabar pressures from x-ray emission spectroscopy, *Phys. Rev. Lett.* **83**, 4101 (1999).
35. Bass, S. A., *et al.*, Microscopic models for ultrarelativistic heavy ion collisions, *Prog. Part. Nucl. Phys.* **41**, 225 (1998).
36. Boguta, J., Baryonic degrees of freedom leading to density isomers, *Phys. Lett. B* **109**, 251 (1982).
37. Li, B.-A., Ko, C.M. and Ren, Z., Equation of state of asymmetric nuclear matter and collisions of neutron-rich nuclei, *Phys. Rev. Lett.* **78**, 1644 (1997).
38. Li, B.-A., Neutron-proton differential flow as a probe of isospin-dependence of the nuclear equation of state, *Phys. Rev. Lett.* **85**, 4221 (2000).
39. Colonna, M., Di Toro, M., Fabbri, G. and Maccarone, S., Effects of charge symmetry on heavy ion reaction mechanisms, *Phys. Rev. C* **57**, 1410 (1998).
40. Tsang, M.B. *et al.*, Isotopic scaling in nuclear reactions, *Phys. Rev. Lett.* **86**, 5023 (2001).

This work was supported by the U.S. National Science Foundation and by the U.S. Department of Energy.

Correspondence and requests for materials should be addressed to W.G.L. (e-mail: lynch@nscl.msu.edu).

FIGURE CAPTIONS:

Figure 1: Overview of the collision dynamics. Various aspects of Au+Au collisions are shown as a function of the elapsed time. In the middle, a three-dimensional view is shown of the locus of points roughly at a density of $\rho=0.1 \rho_0$. The two-dimensional panels at the bottom indicate the calculated density in the reaction plane (x-z plane). The two-dimension panels in the back indicate the calculated pressure in the plane perpendicular to the beam momentum. The various contours in the two dimensional panels are discussed in the text. The arrows indicate average velocities of nucleons in these planes. The center of mass is at $\bar{r} = 0$ and the orientation of the axes is the same for the two-dimensional and three dimension representations.

Figure 2: Transverse flow results. The solid and open points show experimental values for the transverse flow as a function of the incident energy per nucleon. The labels “Plastic Ball”, “EOS”, “E877” and “E895” denote data taken from Gustafsson *et al.*²³, Partlan *et al.*²⁴, Barrette *et al.*²⁵ and Liu *et al.*²⁶, respectively. The various lines are the transport theory predictions for the transverse flow that are discussed in the text.

Figure 3: Zero temperature EOS for symmetric nuclear matter. The cross-hatched region corresponds to the region of pressures consistent with the

experimental flow data. The various curves and lines show predictions for different symmetric matter equations of state that are discussed in the text.

Figure 4: Elliptic flow results. The solid and open points show experimental values for the elliptic flow as a function of the incident energy per nucleon. The labels “Plastic Ball”, “EOS”, “E895” and “E877” denote data of Gutbrod *et al.*²⁷, Pinkenburg *et al.*²⁸, Pinkenburg *et al.*²⁸ and Braun-Munzinger and Stachel²⁹, respectively. The various lines are the transport theory predictions for the elliptic flow that are discussed in the text.

Figure 5: Constraints on the momentum dependence of the mean field. The solid points show experimental values³⁰ for $\langle \cos 2\phi \rangle$ in Bi+Bi peripheral collisions at incident energies of $E = 700$ MeV/nucleon as a function of the transverse momentum of the detected protons. The various lines are transport theory predictions for $\langle \cos 2\phi \rangle$ assuming different momentum dependences for the nuclear mean field¹⁰. The error bars on the theoretical curves indicate the statistical uncertainty in the theoretical calculations.

Figure 6: Zero temperature EOS for neutron matter. The upper and lower shaded regions correspond to the pressure regions for neutron matter consistent with the experimental flow data after the pressures due to asymmetry terms with strong and weak density dependences, respectively, are included. The various curves and lines show predictions for different neutron matter equations of state that are discussed in the text.

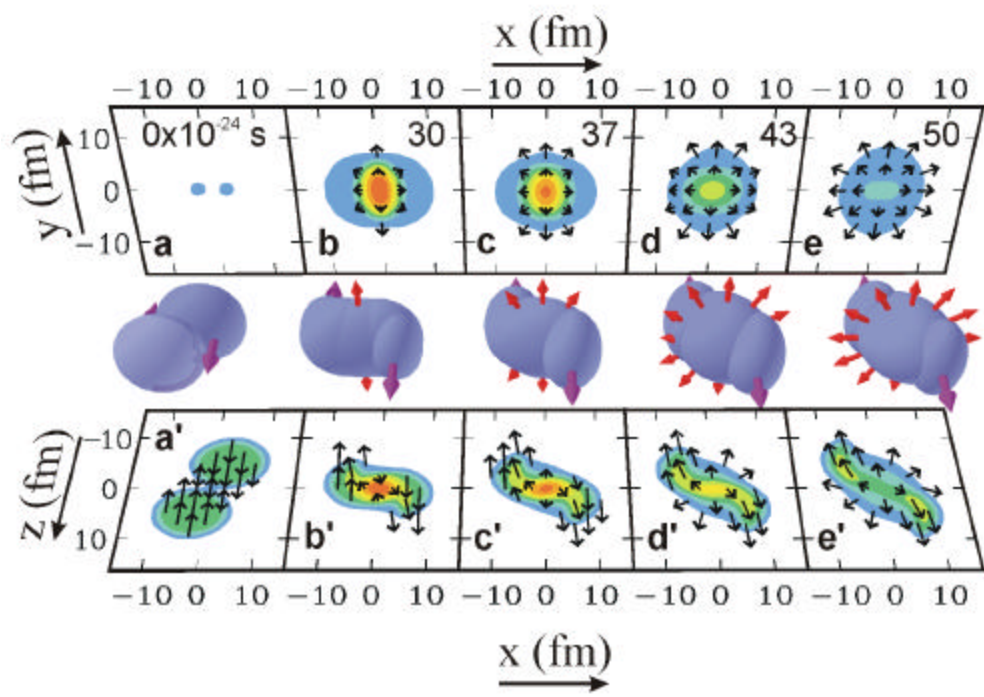


FIGURE 1

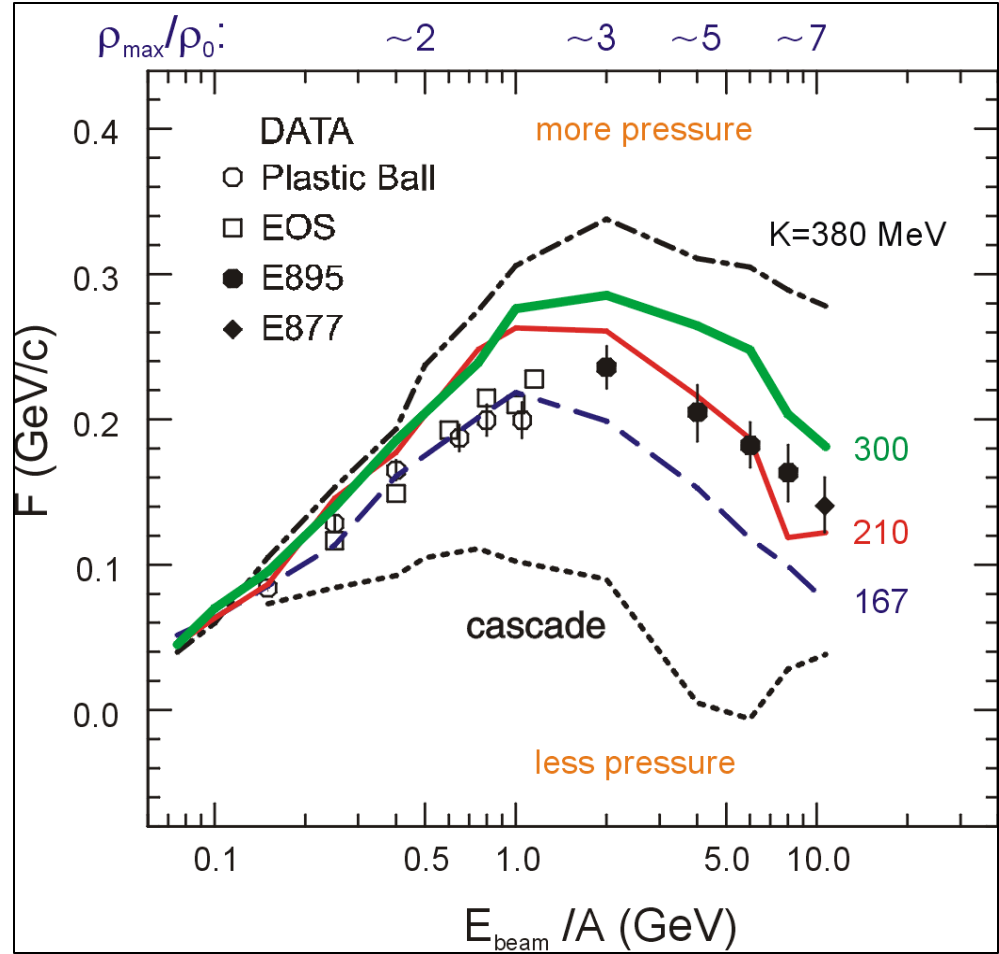


FIGURE 2

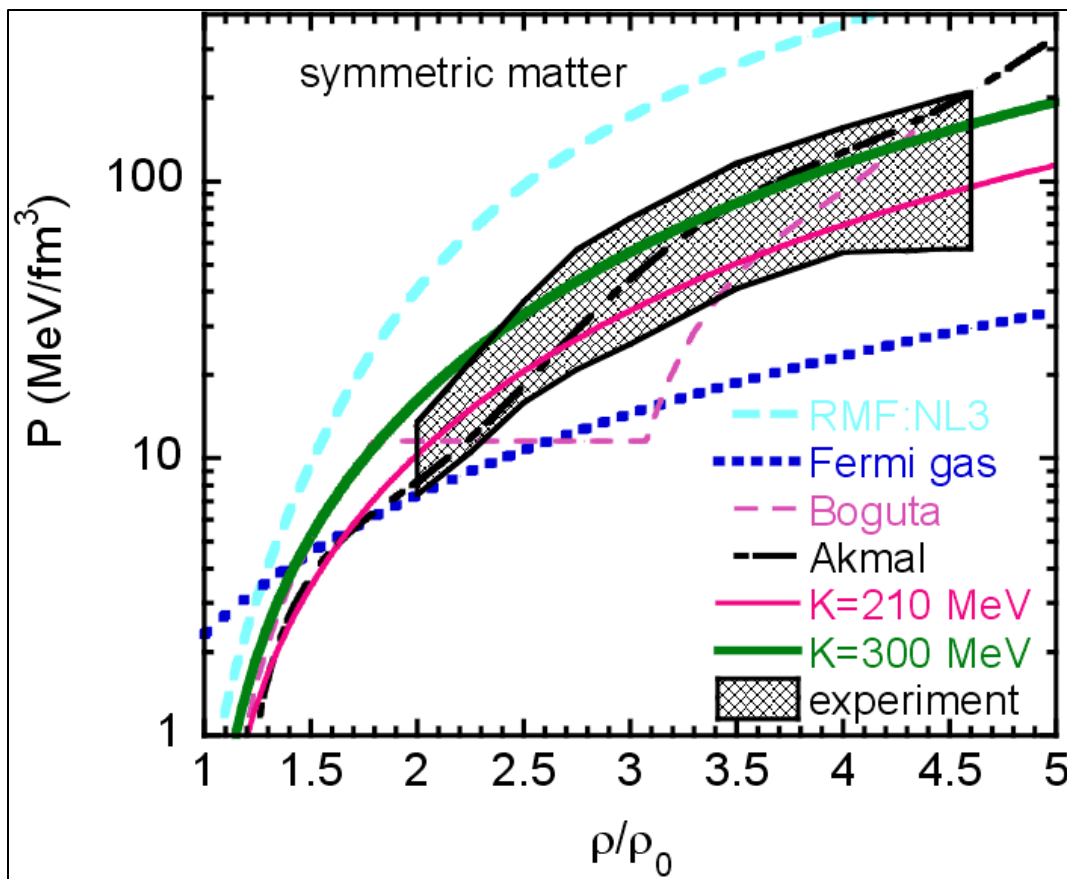


FIGURE 3

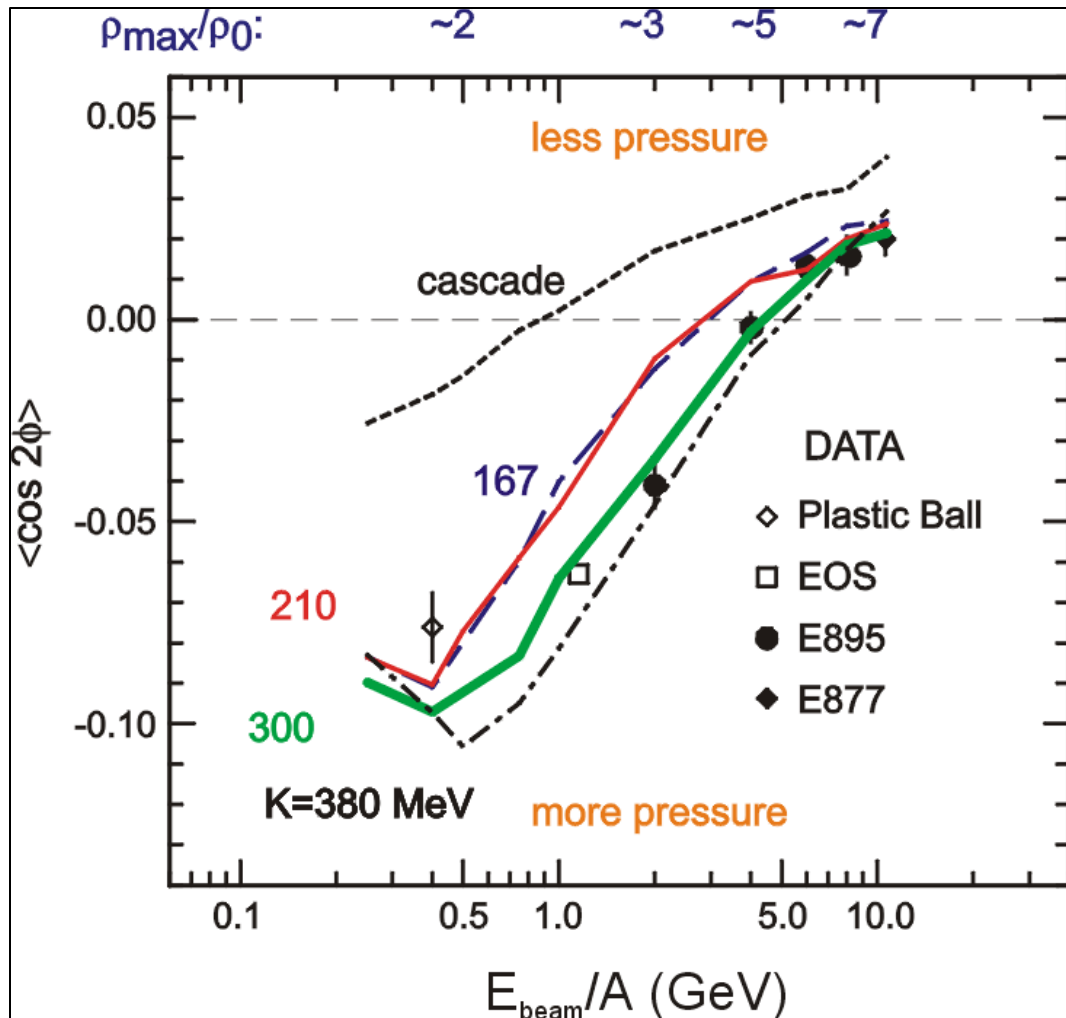


FIGURE 4

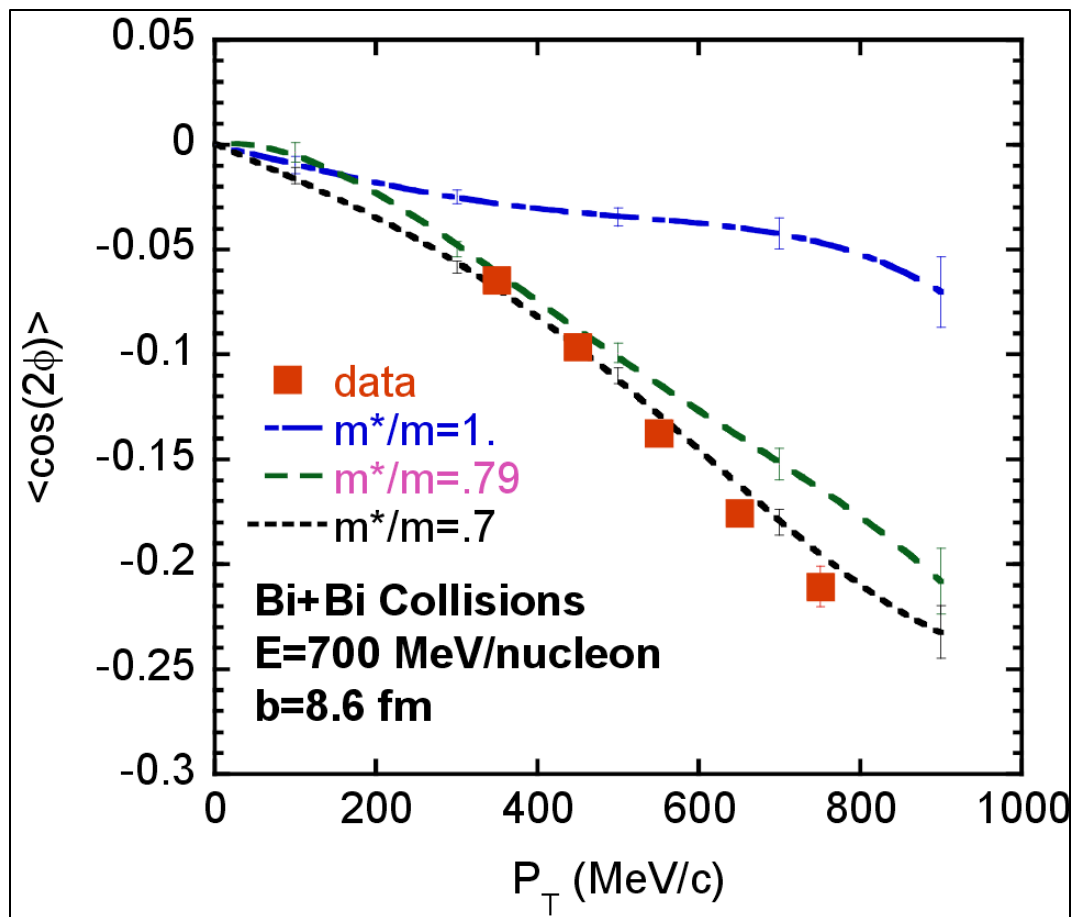


FIGURE 5

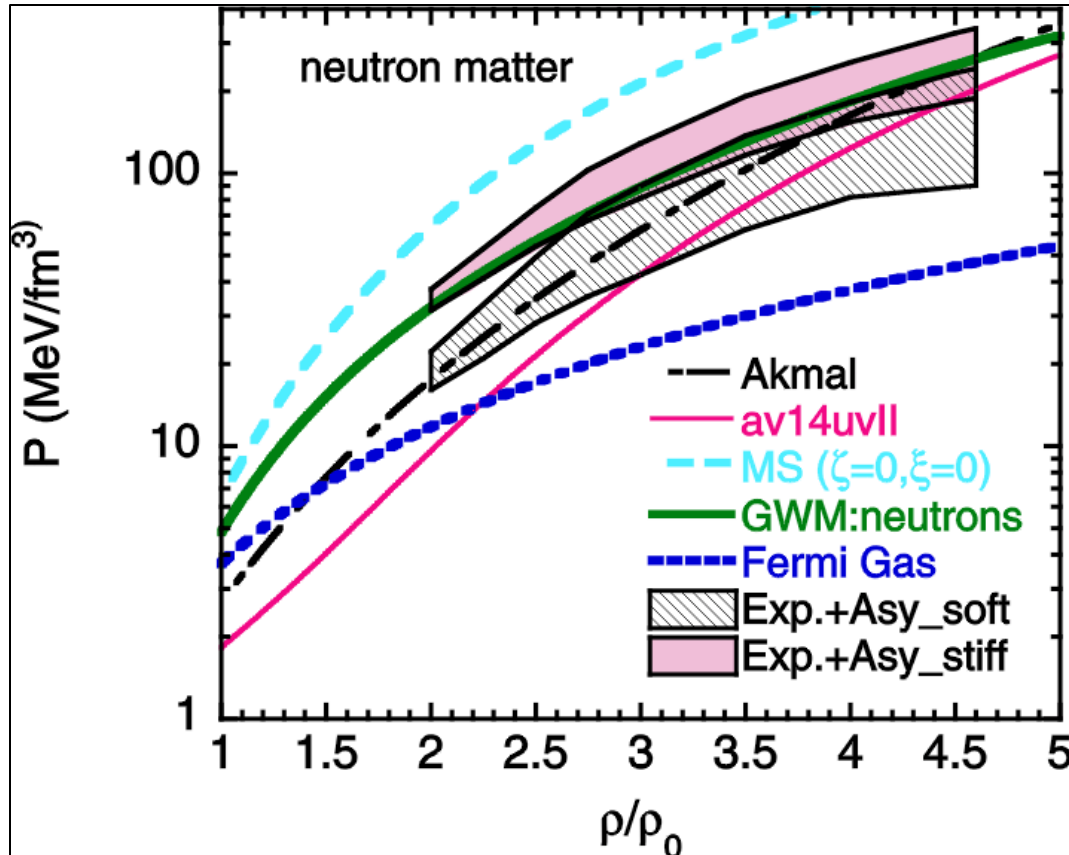


FIGURE 6